

The Heidelberg spiking datasets for the systematic evaluation of spiking neural networks

Benjamin Cramer¹, Yannik Stradmann¹, Johannes Schemmel¹, and Friedemann Zenke²

¹Kirchhoff Institute for Physics, University of Heidelberg, Germany

²Friedrich Miescher Institute for Biomedical Research, Basel, Switzerland

October 26, 2020

Abstract

Spiking neural networks are the basis of versatile and power-efficient information processing in the brain. Although we currently lack a detailed understanding of how these networks compute, recently developed optimization techniques allow us to instantiate increasingly complex functional spiking neural networks in-silico. These methods hold the promise to build more efficient non-von-Neumann computing hardware and will offer new vistas in the quest of unraveling brain circuit function. To accelerate the development of such methods, objective ways to compare their performance are indispensable. Presently, however, there are no widely accepted means for comparing the computational performance of spiking neural networks. To address this issue, we introduce two spike-based classification datasets, broadly applicable to benchmark both software and neuromorphic hardware implementations of spiking neural networks. To accomplish this, we developed a general audio-to-spiking conversion procedure inspired by neurophysiology. Further, we applied this conversion to an existing and a novel speech dataset. The latter is the free, high-fidelity, and word-level aligned Heidelberg digit dataset that we created specifically for this study. By training a range of conventional and spiking classifiers, we show that leveraging spike timing information within these datasets is essential for good classification accuracy. These results serve as the first reference for future performance comparisons of spiking neural networks.

1 Introduction

Spiking neural networks (SNNs) are biology’s solution for fast and versatile information processing. From a computational point of view, SNNs have several desirable properties: They process information in parallel, are noise-tolerant, and highly energy efficient [Boahen, 2017]. Precisely which computations are carried out in a given biological SNN depends in large part on its connectivity structure. To instantiate such functional connectivity in-silico, a growing number of SNNs training algorithms have been developed [Zenke and Ganguli, 2018; Pfeifer and Pfeil, 2018; Tavanaei et al., 2018; Bellec et al., 2018; Shrestha and Orchard, 2018; Woźniak et al., 2020; Neftci et al., 2019] both for conventional computers and neuromorphic hardware [Schemmel et al., 2010; Friedmann et al., 2016; Furber et al., 2013; Davies et al., 2018; Moradi et al., 2018; Roy et al., 2019]. However, this diversity of learning algorithms urgently calls for principled means to compare them. Unfortunately, widely accepted benchmark datasets for SNNs that would permit such comparisons are scarce [Roy et al., 2019; Davies, 2019]. Hence, in this article, we seek to fill this gap by introducing two new broadly applicable classification datasets for SNNs.

In the following, we provide a brief motivation for why benchmarks are crucial before reviewing existing tasks that have been used to assess SNN performance in the past. By analyzing the strengths and shortcomings of these

tasks, we motivate our specific choices for the datasets we introduce in this article. Finally, we establish the first set of baselines by testing a range of conventional and SNN classifiers on these datasets.

1.1 Why benchmarks?

The ultimate goal of a benchmark is to provide a quantitative unbiased way of comparing different approaches and methods to the same problem. While each modeler usually works with a set of *private* benchmarks, tailored to their specific problem of study, it is equally important to have shared benchmarks, which ideally everybody agrees to use, to allow for unbiased comparison and to foster constructive competition between approaches [Roy et al., 2019; Davies, 2019].

The last decades of machine learning research would be hard to imagine without the ubiquitous MNIST dataset [LeCun et al., 1998], for instance. To process MNIST using a SNNs, it has to be transformed into spikes. This transformation step puts comparability at risk by leaving fundamental design decisions to the modeler. Presently, the SNN network community has a shortage of established benchmarks that avoid the conversion step by directly providing spike trains to the end-user. By impeding the quantitative comparison between methods, the lack of suitable benchmarks has the potential to slow down the progress of the SNN research community as a whole.

Since community benchmarks are essential, then why is there little agreement on which benchmark to use? There are several possible reasons, but the most likely ones are the following: First, an existing benchmark may be *un-obtainable*. For instance, it could be unpublished, behind a paywall, or too difficult to use. Second, a published benchmark might be *tailored* to a specific problem and, therefore, not general enough to be of interest to other researchers. Third, a benchmark may be *saturated*, which means that it is already solved with high precision by an existing method. Naturally, this precludes the characterization of improvements over these approaches. Finally, a benchmark could require extensive preprocessing.

The question, therefore, is: What would an ideal benchmark dataset for learning in SNNs be? While this question is difficult, if not impossible, to answer, it is probably fair to say that an ideal benchmark should be at least unsaturated, require minimal preprocessing, be sufficiently general, easy to obtain, and free to use.

1.2 Previous work

There are no unified approaches to measuring performance in SNNs which is partially due to the numerous different learning approaches and architectures. SNN architectures can coarsely be categorized into steady-state rate-coding and temporal coding networks, although also hybrids between the two exist. In steady-state rate-coding, SNNs approximate conventional analog neural networks by using an effective firing rate code in which both input and output firing rates remain constant during the presentation of a single stimulus [Pfeiffer and Pfeil, 2018; Zylberberg et al., 2011; Neftci et al., 2017]. Inputs to the network enter as Poisson distributed spike trains with rates are proportional to the current input level. Similarly, network outputs are given as a firing rate or spike count of designated output units. Because of these input-output specifications, steady-state rate-coding networks can often be trained using network translation [Pfeiffer and Pfeil, 2018] and they can be tested on standard machine learning datasets (e.g. MNIST [LeCun et al., 1998], CIFAR10 [Krizhevsky et al., 2009], or SVHN [Netzer et al., 2011]).

The capabilities of SNNs, however, go beyond such rate-coding networks. In temporally coding networks, input and output activity varies during the processing of a single input example. Within this coding scheme, outputs can be either individual spikes [Gütig, 2014; Bohte et al., 2002; Mostafa, 2018; Comsa et al., 2019], spike trains with predefined firing times [Memmesheimer et al., 2014], varying firing rates [Gilra and Gerstner, 2017; Nicola and Clopath, 2017; Thalmeier et al., 2016], or continuously varying quantities derived from output spikes. The latter are typically defined as linear combinations of low-pass filtered spike trains [Gilra and Gerstner, 2017; Nicola and Clopath, 2017; Eliasmith and Anderson, 2004; Denève and Machens, 2016; Abbott et al., 2016].

One of the simplest temporal coding benchmarks is the temporal exclusive-OR (XOR) task, which exists in different variations [Bohte et al., 2002; Abbott et al., 2016; Huh and Sejnowski, 2018]. A simple SNN without hidden

layers cannot solve this problem, similar to the Perceptron’s inability to solve the regular XOR task. Hence, the temporal XOR is commonly used to demonstrate that a specific method supports hidden-layer learning. In the temporal XOR task, a neural network has to solve a Boolean XOR problem in which the logical *off* and *on* levels correspond to early and late spike times respectively. While the temporal XOR does require a hidden layer to be solved correctly, its intrinsic low-dimensionality and the low number of input patterns render this benchmark saturated. Therefore, its possibilities for quantitative comparison between training methods are limited.

To assess learning in a more fine-grained way, several studies have focused on SNNs’ abilities to generate precisely timed output spike trains in more general scenarios [Memmesheimer et al., 2014; Ponulak and Kasiński, 2009; Pfister et al., 2006; Florian, 2012; Mohemmed et al., 2012; Gardner and Grüning, 2016]. To that end, it is customary to use several Poisson input spike trains to generate a specific target spike train. Apart from regular (e.g. Gardner and Grüning [2016]), also random output spike trains with increasing length and Poisson statistics have been considered [Memmesheimer et al., 2014]. Similarly, the Tempotron [Gütig and Sompolinsky, 2006] uses an interesting hybrid approach in which random temporally encoded spike input patterns are classified into binary categories corresponding to spiking versus quiescence of a designated output neuron. In the associated benchmark, task performance is measured as the number of binary patterns that can be classified correctly. While mapping random input spikes to output spikes allows a fine-grained comparison between methods, the aforementioned tasks lack a non-random structure.

Finally, some datasets for n-way classification were born out of practical engineering needs. The majority of these datasets are based on the output of neuromorphic sensors like, for instance, the dynamic vision sensor (DVS) [Lichtsteiner et al., 2008] or the silicon cochlea [Anumula et al., 2018]. An early example of such a dataset is Neuromorphic MNIST [Orchard et al., 2015], which was generated by a DVS recording MNIST digits that were projected on a screen. The digits were moved at certain intervals to elicit spiking responses in the DVS. The task is to identify the corresponding digits from the elicited spikes. This benchmark has been used widely in the SNN community. However, being based on the MNIST dataset it is nearing saturation. The DASDIGITS dataset [Anumula et al., 2018] was created by processing the TIDIGITS with a 64 channel silicon cochlea. Unfortunately, the license requirements for the derived dataset are not entirely clear as the TIDIGITS are released under a proprietary license. Moreover, because TIDIGITS contains sequences of spoken digits, the task goes beyond a straight-forward n-way classification problem and therefore is beyond the scope for many current SNN implementations. More recently, IBM has released the DVS128 Gesture Dataset [Amir et al., 2017] under a Creative Commons license. The dataset consists of numerous DVS recordings of 11 unique hand gestures performed by different persons under varying lighting conditions. The spikes in this dataset are

provided as a continuous data stream, which makes extensive cutting and preprocessing necessary. Finally, the 128×128 pixel size renders this dataset computationally expensive unless additional preprocessing steps such as downsampling are applied.

In this article, we sought to generate two widely applicable SNN benchmarks with comparatively modest computational requirements. Thus, we focused on audio signals of spoken words due to their natural temporal dimension and lower bandwidth compared to video data and developed a processing framework to convert these audio data into spikes. Using this framework, we generated two spike-based datasets for speech classification and keyword spotting that are not saturated by current methods. Moreover, solving these problems with high accuracy requires taking into account spike timing.

2 Methods

To improve the quantitative comparison between SNNs, we have created two large spike-based classification datasets from audio data. Specifically, we recorded the Heidelberg Digits (HD) dataset for this purpose and used the published Speech Commands (SC) dataset by the TensorFlow and AIY teams [Warden, 2018]. In the following, we describe the datasets (Section 2.1), the audio-to-spike conversion (Section 2.2), and the data format used for publication (Section 2.3). We close with a depiction of the SNN model (Section 2.4). The non-spiking classifiers are outlined in Appendix B. All reported error measures in this work correspond to the standard deviation of 10 experiments.

2.1 Audio datasets

In the following, we consider the Heidelberg Digits (HD) (Section 2.1.1) and the SC dataset (Section 2.1.2). While the HD were optimized for recording quality and precise audio alignment, the SC are intended to closely mimic real-world conditions for key-word spotting on mobile devices.

2.1.1 Heidelberg Digits

The HD¹ consist of approximately 10k high-quality recordings of spoken digits ranging from *zero* to *nine* in English and German language. In total 12 speakers were included, six of which were female and six male. The speaker ages ranged from 21 yr to 56 yr with a mean of (29 ± 9) yr. We recorded around 40 digit sequences for each language with a total digit count of 10 420 (cf. Figure 1).

The digits were acquired in sequences of ten successive digits. Recordings were performed in a sound-shielded room at the Heidelberg University Hospital with three microphones; two AudioTechnica Pro37 in different positions and a Beyerdynamic M201 TG (Figure 2). Digitized by a Steinberg MR816 CSX audio interface, recordings were made in WAVE format with a sample rate of 48 kHz and 24 bit precision.

¹<https://compneuro.net>

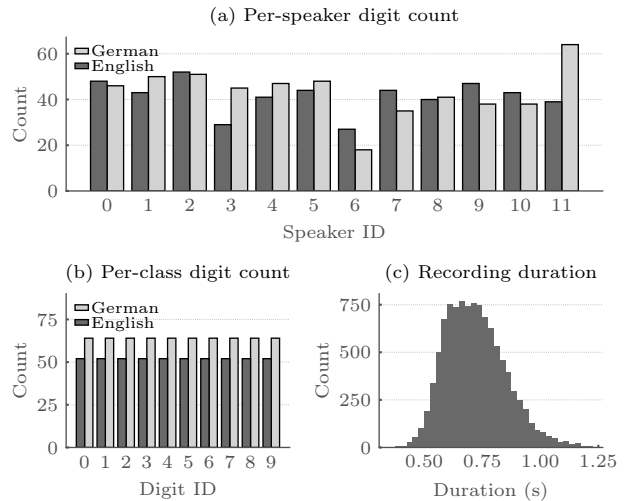


Figure 1: The Heidelberg Digits (HD) have a balanced class count and variable temporal duration. The HD consist of 10420 recordings of spoken digits ranging from *zero* to *nine* in English and German language. (a) Histogram of per-speaker digit counts. Variable numbers of digits are available for each speaker and each language. (b) Histogram of per-class digit counts. The dataset is balanced in terms of digits within each language. (c) Histogram of audio recording durations. The HD audio recordings were cut for minimal duration to keep computation time at bay.

To improve the yield of the following automated processing, a manual pre-selection and cutting of the raw audio tracks were performed accompanied by conversion to Free Lossless Audio Codec (FLAC) format. The cleaned-up tracks were externally mastered [Schumann]. The cutting times of the digit sequences were determined using a gate with speaker-dependent threshold and release time which were optimized by the blackbox-optimizer described in Knysh and Korkolis [2016]. The loss function was designed to produce 10 single files with the lowest possible threshold and shortest gate opening to prevent unnecessary computation during successive analysis and modeling. Additionally, speaker-specific ramp-in and ramp-out times were determined by visual inspection. The final digit files differ in duration due to speaker differences (Figure 1). 30 ms Hann windows were applied to the start and end of the peak normalized audio signals as further processing stages involve the computation of fast Fourier transformations (FFTs).

To separate the data into training and test sets, we held out two speakers exclusively for the test set. The remainder of the test set was filled with samples (5% of the trials) from speakers also present in the training set. This division allows to assess a trained network’s ability to generalize across speakers.

2.1.2 Speech Commands

The SC² are composed of 1 s WAVE-files with 16 kHz sample rate containing a single English word each [Warden, 2018]. It is published under *Creative Commons BY 4.0* license and contains words spoken by 1864 speakers. In

²<https://www.tensorflow.org>

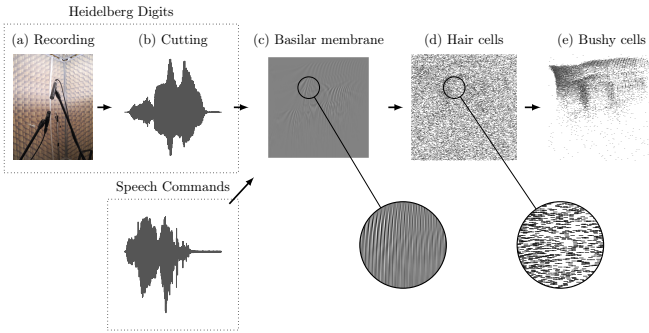


Figure 2: Processing pipeline for the HD and the SC dataset. (a) The HD are recorded in a sound-shielded room. (b) Afterwards, the resulting audio files are cut and mastered. (c) The HD as well as the SC are fed through a hydrodynamic basilar membrane model. (d) Basilar membrane decompositions are converted to phase-coded spikes by use of a transmitter-pool based hair cell model. (e) The phase-locking is increased by combining multiple spiketrains of hair cells at the same position of the basilar membrane in a single bushy cell.

this study, we considered version 0.02 with 105 829 audio files, in which a total of 24 single word commands (*Yes, No, Up, Down, Left, Right, On, Off, Stop, Go, Backward, Forward, Follow, Learn, Zero, One, Two, Three, Four, Five, Six, Seven, Eight, Nine*) were repeated about five times per speaker, whereas ten auxiliary words (*Bed, Bird, Cat, Dog, Happy, House, Marvin, Sheila, Tree, and Wow*) were only repeated approximately once. Partitioning into training, testing and validation dataset was done by a hashing function as described in Warden [2018].

For all our purposes, we applied a 30 ms Hann window to the start and end of each waveform. Most importantly, throughout this article we consider top one classification performance on all 35 different classes which is more difficult than the originally proposed key-word spotting task on only a subset of 12 classes (10 key-words, unknown word, and silence). However, the data can still be used in the originally intended keyword spotting way.

2.2 Spike conversion

The audio files described above served as the basis for our spiking datasets. Audio data were converted into spikes using an artificial model³ of the inner ear and parts of the ascending auditory pathway (Figure 2; Appendix A). This biologically inspired model effectively performs similar signal processing steps as customary spoken language processing applications [Huang et al., 2001]. First, a hydrodynamic basilar membrane (BM) model (Appendix A.1) causes spatial frequency dispersion, which is comparable to computing a spectrogram with Mel-spaced filter banks. Second, these separated frequencies are converted to firing rates through a biologically motivated transmitter pool based hair cell (HC) model (Appendix A.2), which adds refractory effects, and a layer of bushy cells (BCs) (Appendix A.3) that increase phase locking (cf. Figure 2). All model parameters were

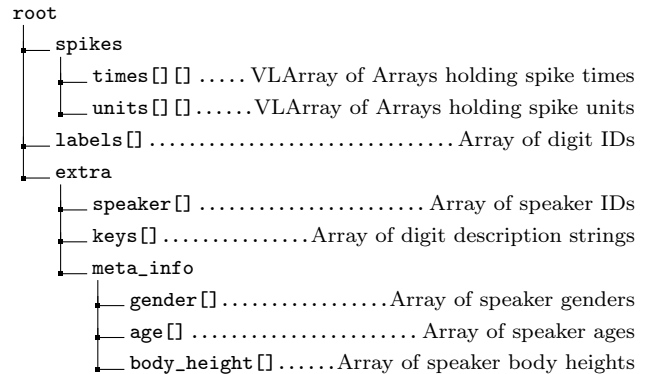
³<https://github.com/electronicvisions/lauscher>

chosen to mimic biological findings, thereby reducing the amount of free parameters (see Table 2).

Overall, the inner-ear model approximates the spiking activity observed in the auditory system while retaining a low computational cost. This biologically inspired conversion allowed us to sidestep the issue of user-specific audio-to-spike transformation, which can confound comparability, and served as the basis for our benchmark datasets.

2.3 Event-based data format

We used an event-based representation of spikes in the Hierarchical Data Format 5 (HDF5) to facilitate the use of the datasets and to simplify the access to a broader community. This choice was to ensure short download times and ease of access from most common programming environments. For each partition and dataset, we provide a single HDF5 file which holds spikes, digit labels, and additional meta information. We made these files publicly available² [Cramer et al., 2019], together with supplementary information on the general usage as well as code snippets. A single file is organized as follows:



In more detail, each element i in $keys$ describes the transformation between the digit ID i and the spoken words. Further, the entry i of each array in $meta_info$ corresponds to the information for speaker i . The $meta_info$ is only available for Spiking Heidelberg Digits (SHD).

2.4 Spiking network models

We trained networks of leaky integrate-and-fire (LIF) neurons with surrogate gradients and backpropagation through time (BPTT) using supervised loss functions to establish a performance reference on the two spiking datasets. In the following we give a description of the network architectures (Section 2.4.1), followed by the applied neuron and synapse model (Section 2.4.2). We close with a depiction of the weight initialization (Section 2.4.3), the supervised learning algorithm (Section 2.4.4) and the loss function (Section 2.4.5) as well as the regularization techniques (Section 2.4.6).

2.4.1 Network model

The spiketrains emitted by the $N_{ch} = 700$ BCs were used to stimulate the actual classification network. In this manuscript, we trained both feed-forward and recurrent networks; each hidden layers containing $N = 128$ LIF

neurons. For all network architectures, the last layer was accompanied by a linear readout consisting of leaky integrators which did not spike.

2.4.2 Neuron and synapse models

We considered LIF neurons where the membrane potential $u_i^{(l)}$ of the i -th neuron in layer l obeys the differential equation:

$$\tau_{\text{mem}} \frac{du_i^{(l)}}{dt} = -[u_i^{(l)}(t) - u_{\text{leak}}] + RI_i^{(l)}(t), \quad (1)$$

with the membrane time constant τ_{mem} , the input resistance R , the leak potential u_{leak} , and the input current $I_i^{(l)}(t)$. Spikes were described by their firing time. The k -th firing time of neuron i in layer l is denoted by ${}_k t_i^{(l)}$ and defined by a threshold criterion:

$${}_k t_i^{(l)} : u_i^{(l)}({}_k t_i^{(l)}) \geq u_{\text{thres}}. \quad (2)$$

Immediately after ${}_k t_i^{(l)}$, the membrane potential is set to the leak potential $u_i^{(l)}(t) = u_{\text{leak}}$. The synaptic input current onto the i -th neuron in layer l was generated by the arrival of presynaptic spikes from neuron j , $S_j^{(l)}(t) = \sum_k \delta(t - {}_k t_j^{(l)})$. A common first-order approximation to model the time course of synaptic currents are exponentially decaying currents which sum linearly [Gerstner and Kistler, 2002]:

$$\frac{dI_i^{(l)}}{dt} = -\frac{I_i^{(l)}(t)}{\tau_{\text{syn}}} + \sum_j W_{ij}^{(l)} S_j^{(l-1)}(t) + \sum_j V_{ij}^{(l)} S_j^{(l)}(t), \quad (3)$$

where the sum runs over all presynaptic partners j and $W_{ij}^{(l)}$ are the corresponding afferent weights from the layer below. The $V_{ij}^{(l)}$ resemble the recurrent connections within each layer.

In this work, the reset was incorporated in Equation (1) through an extra term:

$$\frac{du_i^{(l)}}{dt} = -\frac{u_i^{(l)} + u_{\text{leak}} - RI_i^{(l)}}{\tau_{\text{mem}}} + S_i^{(l)}(t)(u_{\text{leak}} - u_{\text{thres}}). \quad (4)$$

To formulate the above equations in discrete time for time step n and stepsize δt over a duration $T = n \cdot \delta t$, the output spiketrain $S_i^{(l)}[n]$ of neuron i in layer l at time step n is expressed as a nonlinear function of the membrane potential $S_i^{(l)}[n] = \Theta(u_i^{(l)} - u_{\text{thres}})$ with the Heavyside function Θ . For small time steps δt we can express the synaptic current in discrete time as follows:

$$I_i^{(l)}[n+1] = \kappa I_i^{(l)}[n] + \sum_j W_{ij}^{(l)} S_j^{(l)}[n] + \sum_j V_{ij}^{(l)} S_j^{(l)}[n]. \quad (5)$$

Further, by asserting $u_{\text{leak}} = 0$ and $u_{\text{thres}} = 1$, the membrane potential can be written compactly as:

$$u_i^{(l)}[n+1] = \lambda u_i^{(l)}[n](1 - S_i^{(l)}[n]) + (1 - \lambda)I_i^{(l)}[n], \quad (6)$$

where we have set $R = (1 - \lambda)$ and introduced the constants $\kappa \equiv \exp(-\delta t/\tau_{\text{syn}})$ and $\lambda \equiv \exp(-\delta t/\tau_{\text{mem}})$.

2.4.3 Weight initialization

In all our spiking network simulations we use Kaiming's uniform initialization [He et al., 2015] for the weights W_{ij} and V_{ij} . Specifically, the initial weights were drawn independently from a uniform distribution $\mathcal{U}(-\sqrt{k}, \sqrt{k})$ with $k = (\# \text{ afferent connections})^{-1}$.

2.4.4 Supervised learning

The goal of learning was to minimize a cost function \mathcal{L} over the entire dataset. To achieve this, surrogate gradient descent was applied which modifies the network parameters W_{ij} :

$$W_{ij} \leftarrow W_{ij} - \eta \frac{\partial \mathcal{L}}{\partial W_{ij}}, \quad (7)$$

with the learning rate η . In more detail, we used custom PyTorch [Paszke et al., 2017] code implementing the SNNs. Surrogate gradients were computed using PyTorch's automatic differentiation capabilities by overloading the derivative of the spiking nonlinearity with a differentiable function as described previously [Neftci et al., 2019; Zenke and Vogels, 2020]. An instructive example of such an implementation in PyTorch can be found online ⁴. Specifically, we chose a fast sigmoid to calculate the surrogate gradient:

$$\sigma(u_i^{(l)}) = \frac{u_i^{(l)}}{1 + \beta |u_i^{(l)}|}, \quad (8)$$

with the steepness parameter β .

2.4.5 Loss functions

We applied a cross entropy loss to the activity of the readout layer $l = L$. On data with N_{batch} samples and N_{class} classes, $\{(\mathbf{x}_s, \mathbf{y}_s) | s = 1, \dots, N_{\text{batch}}; \mathbf{y}_s \in \{1, \dots, N_{\text{class}}\}\}$ it takes the form:

$$\mathcal{L} = -\frac{1}{N_{\text{batch}}} \sum_{s=1}^{N_{\text{batch}}} \mathbf{1}(i = y_s) \cdot \log \left\{ \frac{\exp(u_i^{(L)}[\tilde{n}_i])}{\sum_{i=1}^{N_{\text{class}}} \exp(u_i^{(L)}[\tilde{n}_i])} \right\}, \quad (9)$$

with the indicator function $\mathbf{1}$. We tested to the following two choices for the time step \tilde{n} (Figure 4): For the *max-over-time* loss, the time step with maximal membrane potential for each readout unit was considered $\tilde{n}_i = \operatorname{argmax}_n u_i^{(L)}[n]$. In contrast, the last time step T for all samples was chosen for each readout neuron $\tilde{n}_i = T$ in case of the *last-time-step* loss. We minimized the cross entropy in Equation (9) using the Adamax optimizer [Kingma and Ba, 2014].

⁴<https://github.com/fzenke/spytorch>

2.4.6 Regularization

For our experiments, we added synaptic regularization terms to the loss function to avoid pathologically high or low firing rates. In more detail, we used two different regularization terms: As a first term, we used a per neuron lower threshold spike count regularization of the form:

$$\mathcal{L}_1 = \frac{s_l}{N_{\text{batch}} + N} \sum_{s=1}^{N_{\text{batch}}} \sum_{i=1}^N \left[\max \left\{ 0, \frac{1}{T} \sum_{n=1}^T S_i^{(l)}[n] - \theta_l \right\} \right]^2, \quad (10)$$

with strength s_l , and threshold θ_l . Second, we used an upper threshold mean population spike count regularization:

$$\mathcal{L}_2 = \frac{s_u}{N_{\text{batch}}} \sum_{s=1}^{N_{\text{batch}}} \left[\max \left\{ 0, \frac{1}{N} \sum_{i=1}^N \sum_{n=1}^T S_i^{(l)}[n] - \theta_u \right\} \right]^2, \quad (11)$$

with strength s_u , and threshold θ_u .

3 Results

To analyze the relevance of our newly created spiking datasets we first sought to establish that the datasets were not saturated and that spike timing information is essential to solve the tasks with high accuracy. To test this, we first generated a reduced version of the datasets in which we removed all temporal information. To that end, we computed spike count patterns from both datasets, which, by design, do not contain temporal information about the stimuli. Using these reduced spike count datasets, we then trained different linear and nonlinear support vector machine (SVM) classifiers (Appendix B.1) and measured their classification performance on the respective test sets. We found that while a linear SVM readily overfitted the data in the case of SHD, its test performance only marginally exceeded the 55% accuracy mark (Figure 3a). For the Spiking Speech Commands (SSC), overfitting was less pronounced, but also the overall test accuracy dropped to 20% (Figure 3b). Thus linear classifiers provided a low degree of generalization.

To assess whether this situation was different for nonlinear classifiers, we trained SVMs with polynomial kernels up to a degree of 3. For these kernels, overfitting was less pronounced. Slightly better performance of about 60% on the SHD and 30% on the SSC was achieved when using a SVM with a radial basis function (RBF) kernel. The performance on the SHD test set, which includes speakers that are not part of the training set, was noticeably lower compared to the accuracy on the validation data. Especially, for polynomial and RBF kernels the generalization across speakers was worse than for the linear kernel (Figure 3a). In contrast, we found the performance on the SSC test set to be on par with the accuracy on the

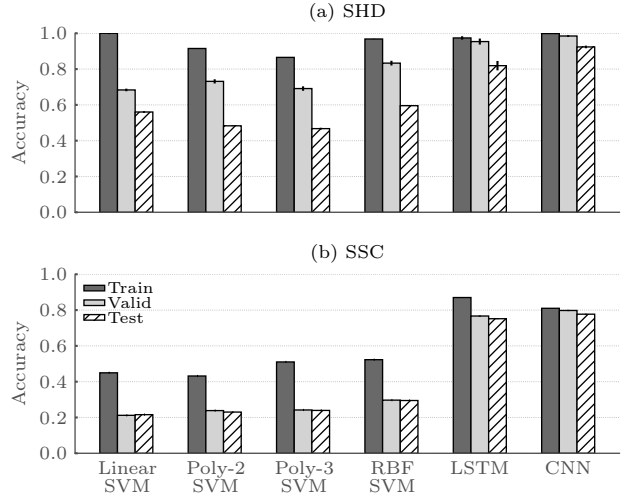


Figure 3: Temporal information is essential to classify the SHD and the SSC datasets with high accuracy. (a) Bar graph of classification accuracy for different SVMs trained on spike count vectors and LSTM as well as CNN classifiers trained on the binned spiketrains of the SHD dataset. Classification accuracy on SHD is substantially higher for LSTMs and CNNs which also show a lower degree of overfitting. (b) Same as in (a), but showing performance on SSC. LSTMs and CNNs with access to temporal information outperform the SVM classifiers by a large margin.

validation set (Figure 3b), which is most likely an effect of the uniform speaker distribution. These results illustrate that both linear and nonlinear classifiers trained on spike count patterns without temporal information were unable to surpass the 60% accuracy mark for the SHD and the 30% mark for the SSC dataset. Therefore, spike counts are not sufficient to achieve high classification accuracy on the studied datasets.

Next, we wanted to assess whether decoding accuracy could be improved when training classifiers that have explicit access to temporal information of the spike times. Therefore, we trained LSTMs on temporal histograms of spiking activity (Appendix B.2). In spite of the small size of the SHD dataset, LSTMs showed reduced overfitting and were able to solve the classification problem with an accuracy of $(85.7 \pm 1.4)\%$ (Figure 3a) which was substantially higher than the best performing SVM. Similarly, for the SSC dataset the LSTM test accuracy $(75.0 \pm 0.2)\%$ was more than twice as high as the best-performing classifier on the spike count data. However, the degree of overfitting was slightly higher than on SHD.

Since both, kernel machines and LSTMs, were affected by overfitting, we tested whether performance could be increased with convolutional neural networks (CNNs) due to their inductive bias on translation invariance in both frequency and time and their reduced number of parameters. To that end, we binned spikes in spatio-temporal histograms and trained a CNN classifier (Appendix B.3). CNNs showed the least amount of overfitting among all tested classifiers; the accuracy dropped by only 1.4% on SHD and by 1.5% on SSC (Figure 3). Especially, the performance on the SHD test data was on par with the one on the validation set, demonstrating a high degree of

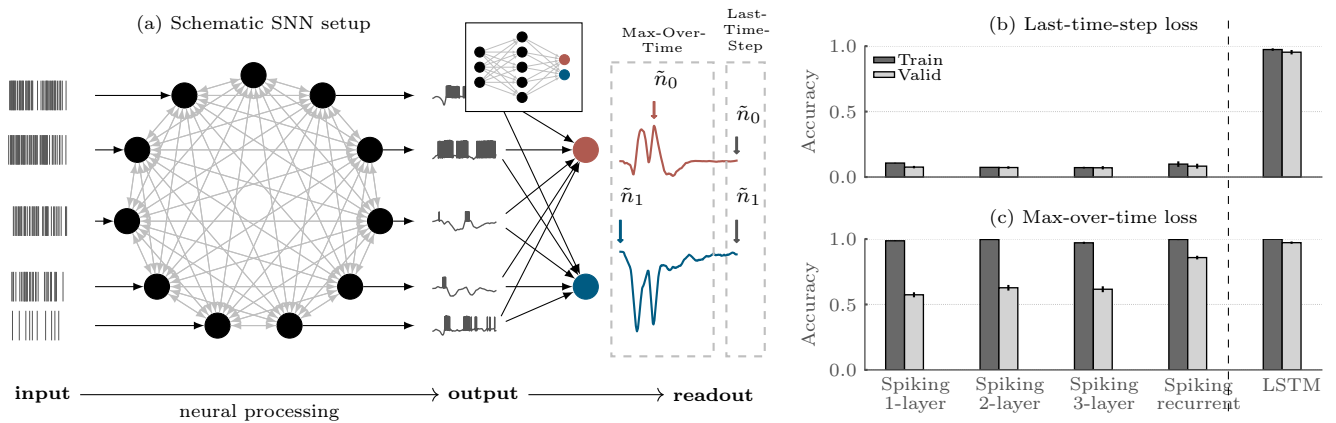


Figure 4: Setup and multiple choices of loss functions for SNNs. (a) Schematic of a single layer recurrent network with two readout units. We applied two different loss functions for long short-term memories (LSTMs) and SNNs: First, a max-over-time loss was considered, where the time step with maximal activity of each readout was used to calculate the cross entropy (marked by colored arrows). Second, a last-time-step loss was utilized where only the last time step of the activation was considered in the calculation of the cross entropy (marked by gray arrow). The inset illustrates the corresponding feed-forward topology. (b) Bar graph of classification accuracy for different SNNs and a LSTM on the SHD. Only the LSTM generalized well when trained with a last-time-step loss. (c) Same as in (b), but showing performance for a max-over-time loss. Overall, SNNs and LSTMs performed better when trained with the max-over-time loss.

generalisation.

These findings highlight that the temporal information contained in both datasets can be exploited by suitable neural network architectures. Moreover, these results provide a lower bound on the performance ceiling for both datasets. It seems likely that a more careful architecture search and hyperparameter tuning will only improve upon these results. Thus, both the SHD and the SSC will be useful for quantitative comparison between SNNs up to at least these empirical accuracy values.

3.1 Training spiking neural networks

Having established that both spiking datasets contain useful temporal information that can be read out by a suitable classifier, we sought to train SNNs of LIF neurons using BPTT to establish a first set of baselines and to assess their generalization properties. One problem with training SNNs with gradient descent arises because the derivative of the neural activation function appears in the evaluation of the gradient. Since spiking is an intrinsically discontinuous process, the resulting gradients are ill-defined. To nevertheless train networks of LIF neurons using supervised loss functions, we used a surrogate gradient approach [Nefcici et al., 2019]. Surrogate gradients can be seen as a continuous relaxation of the real gradients of a SNN which can be implemented as an in-place replacement while performing BPTT. Importantly, we did not change the neuron model and the associated forward-pass of the model, but used a fast sigmoid as a surrogate activation function when computing gradients (Methods Section 2.4.4).

Although not a requirement [Nefcici et al., 2019; Li et al., 2020], we only considered SNNs with fixed, finite time constants on the order of ms inspired by biology. Because of this constraint, we investigate two different loss functions for both LSTMs and SNNs (Figure 4a). The results

for LSTMs shown in Figure 3 were obtained by training with a *last-time-step loss*, where the activation of the last time step of each example and readout unit was used to calculate the cross entropy loss at the output. In addition, we also considered a *max-over-time loss*, in which the time step with maximum activation of each readout unit was taken into account (Figure 4a). This loss function is motivated by the Tempotron [Gütig and Sompolinsky, 2006] in which the network signals its decision about the class membership of the applied input pattern by whether a neuron spiked or not.

We evaluated the performance of LSTMs and SNNs for both aforementioned loss functions on the SHD. Training LSTMs with a cross entropy loss based on the activity of the last time step of every sample was associated with high performance in contrast to SNNs (Figure 4b). The slightly reduced performance of feed-forward SNNs trained with last-time-step loss compared to recurrently connected spiking neural networks (RSNNs) suggests that time constants were too low to provide all necessary information at the last time step. This was presumably due to active memory implemented through reverberating activity through the recurrent connections. Overall, SNNs performed better in combination with the max-over-time loss function (Figure 4c). Also LSTMs showed increased performance in combination with a max-over-time loss; the validation accuracy increased from $(95.4 \pm 1.7) \%$ for the last-time-step loss to $(97.2 \pm 0.9) \%$ for the max-over-time loss. Motivated by these results, we used a max-over-time loss for SNNs as well as LSTMs throughout the remainder of this manuscript.

Surrogate gradient learning introduces a new hyperparameter β associated with the steepness of the surrogate derivative (Methods Equation (7)). Because changes in β may require a different optimal learning rate η , we performed a grid search over β and η based on a single-layer RSNN architecture trained on SHD. We found that

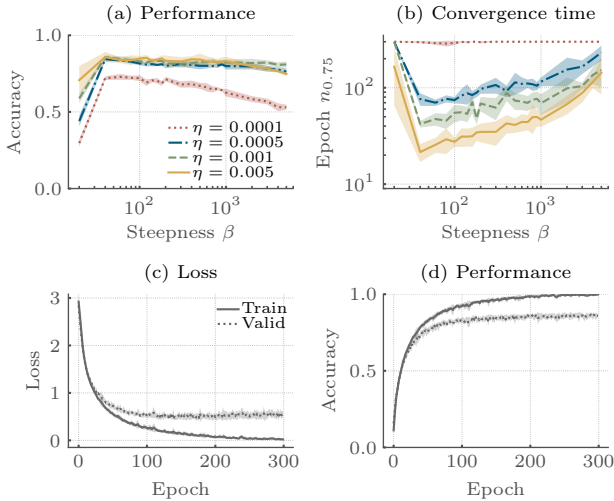


Figure 5: Accuracy, but not convergence time is only mildly affected by the steepness β of the surrogate derivative. (a) Accuracy as a function of β on a validation set of the SHD for different learning rates η . Performance is highest for a wide range of β values ($\beta \geq 40$) and depends only slightly on η . (b) Number of epochs needed to reach an accuracy > 0.75 , $n_{0.75}$. In contrast to the performance, $n_{0.75}$ strongly depends on both β and η . (c) Loss curves on the SHD for $\beta = 40$ and $\eta = 10^{-3}$. (d) Same as in (c), but showing the accuracy on the SHDs.

sensible combinations for both parameters lead to stable performance plateaus over a large range of values (Figure 5a). Only for small β the accuracy dropped dramatically, whereas it decreased only slowly for high values. Interestingly, the learning rate had hardly any effect on peak performance for the tested parameter values. As expected, convergence speed heavily depended on both η and β . These results motivated us to use $\beta = 40$ and $\eta = 1 \times 10^{-3}$ for all SNNs architectures presented in this article unless mentioned otherwise. For this choice, the performance of the RSNN on the validation set reached its peak after about 150 epochs (Figure 5d). Additional training only increased performance on the training dataset (Figure 5c), but did not impact generalization (Figure 5d).

With the parameter choices discussed above, we trained various SNN architectures on the SHD and the SSC. To that end, we considered multi-layer feed-forward SNNs with l layers and a single-layer RSNN. Interestingly, increasing the number of hidden layers l did not notably improve performance on the SHD (Figure 6a). In addition, all choices of l caused high levels of overfitting. Moreover, feed-forward SNNs reached slightly lower accuracy levels than the SVMs on the SHD (Figure 3a). For the larger SSC dataset, the degree of overfitting was much smaller (Figure 6b) and performance was markedly better than the one reached by SVMs (Figure 3b). Here, increasing the number of layers of feed-forward SNNs led to a monotonic increase of performance on the test set from $(32.5 \pm 0.5)\%$ for a single layer to $(41.0 \pm 0.5)\%$ in the three-layer case ($l = 3$). However, when testing RSNNs, we found consistently higher performance and improved generalization across speakers. In comparison to the accuracy of LSTMs, RSNNs showed higher overfitting, and

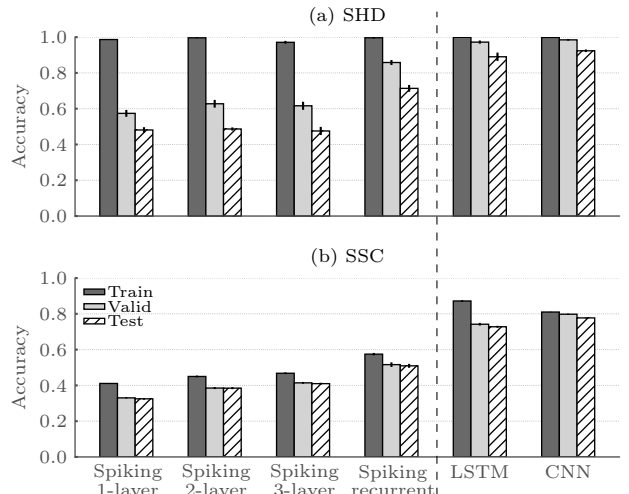


Figure 6: Recurrent SNNs outperform feed-forward architectures on both datasets. (a) Bar graph of classification accuracy for different SNN architectures on the SHD. The accuracy reached by RSNN is comparable to the performance of LSTMs with a max-over-time loss. Increasing the number of layers in feed-forward architectures hardly affected performance. (b) Same as in (a), but showing performance on the SSC. The performance of SNNs was lower than the one reached by LSTMs. In contrast to (a), an increasing number of layers lead to a monotonic increase of accuracy.

generalized less well across speakers. The RSNN achieved the highest accuracy of $(71.4 \pm 1.9)\%$ on the SHD and $(50.9 \pm 1.1)\%$ on the SSC which was still less than the LSTM with $(85.7 \pm 1.4)\%$ on the SHD and $(75.0 \pm 0.2)\%$ on the SSC.

3.2 Generalization across speakers and datasets

For robust spoken word classification, the generalization across speakers is a key feature. This generalization can be assessed by evaluating the accuracy per speaker on SHD, as the digits spoken by speakers four and five are only present in the test set. We compared the performance on the digits of the held-out speakers to all other speakers and found a clear performance drop across all classification methods for the speakers four and five (Figure 7a and c). For SVMs, the linear kernel led to the smallest accuracy drop of about 18%, whereas we found a decrease of 26% for the RBF kernel. CNNs generalized best with a drop of only 8%, followed by the LSTMs with 10%. Among SNNs, feed-forward architectures were most strongly affected with a drop of about 24% to 27%. RSNNs, however, only underwent a decline of 21% in performance (Figure 7b). This illustrates that the composition of the test set of SHD can provide meaningful information with regard to generalization across speakers.

Because English digits are part of both datasets, we were able to test the generalization across datasets by training SNNs, LSTM and CNNs on the full SHD dataset while testing on a restricted SSC dataset and vice versa (Figure 7b and d). For testing, the datasets were restricted to the common English digits *zero* to *nine*. Perhaps not

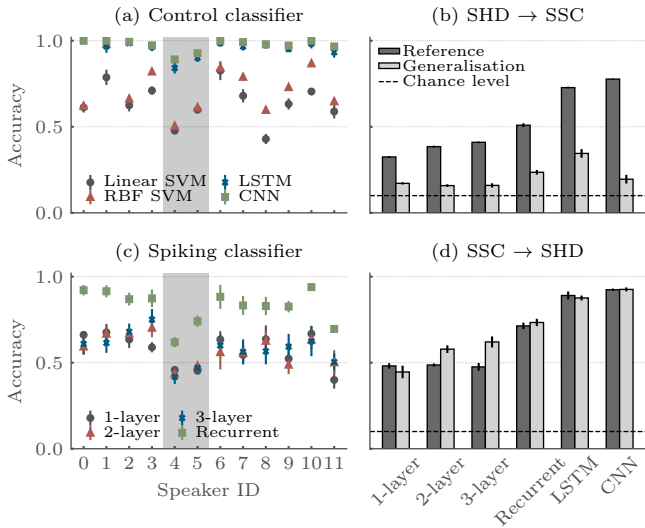


Figure 7: Networks generalize across speakers and datasets. By reserving two speakers for the test set, the SHD dataset allows to assess speaker generalization performance. (a) Per-speaker classification accuracy on the test set of the SHD for different classifiers. A clear decrease in performance was observable for samples spoken by the held-out speakers four and five (highlighted). (b) Bar graph of the performance of SNNs, LSTM and CNN trained on the SHD and tested on the English digits of the SSC. The reference is given by the performance on the SHD test set, and the generalisation by the performance on the English digits of the SSC test set. Accuracy on the SSC digits was substantially lower than on the digits in the SSC test set. (c) Same as in (a), but showing the per-speaker accuracy of SNNs. As for (a), a decrease in performance for the held-out speakers was observed. (d) Same as in (b), but showing the performance of networks when trained on SSC and tested on the English digits of the SHD. As opposed to (b), networks trained on the SSC digits generalize well across datasets.

surprisingly, networks generalized better, when trained on the larger SSC dataset as a reference and tested on SHD. Nevertheless, all architectures trained on the SHD and tested on the SSC reached performance levels above chance. Again, recurrent architectures reached highest performance among all tested SNNs.

3.3 Improving generalization performance through data augmentation and larger networks

We first tested the effect of network size on the generalization performance of the RSNN architecture using the smaller SHD dataset. As expected, we found that increasing the network size up to 1024 neurons indeed resulted in improved validation and test accuracy up to $(76.5 \pm 1.0)\%$ with 1024 neurons (Figure 8a).

Next, we compressed the input in terms of channels, since a similar modification led to good results for the CNNs (cf. Figure 6). To that end, we coarse-grained the inputs by condensing the spike trains of neighboring input units. Merging 10 neighboring channels did improve validation accuracy with an associated test accuracy of $(72.2 \pm 1.6)\%$ (Figure 8b). This choice resulted

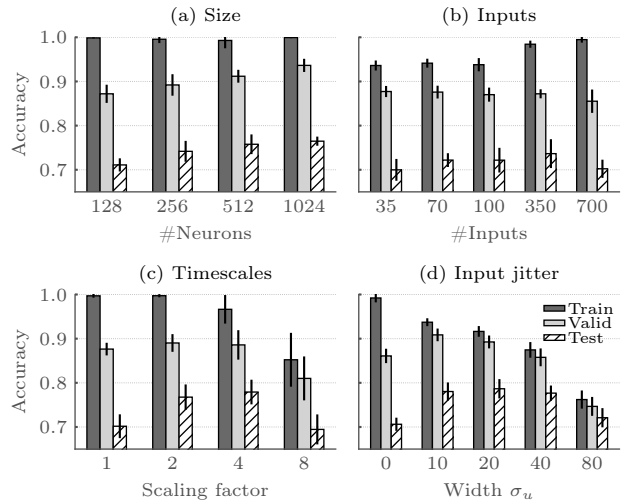


Figure 8: Generalization performance improves with network size and data augmentation. (a) Bar graph of classification accuracy for different network sizes. Larger networks generalize best. (b) Same as before, but showing the accuracy for different numbers of input channels. Networks generalized best when the spikes of the 700 input units were compressed to 70 units. (c) Network performance for temporally scaled synaptic and membrane time constants. Highest performance on the validation set was reached for an expansive scaling factor of 4. (d) Classification accuracy for spatially noisy (channel jitter) input spikes. An optimum occurs for a standard deviation of $\sigma_u = 20$ channels.

in an overall channel count of 70. Despite the only slight increase in test accuracy, the corresponding networks with fewer channels benefited from a smaller computational footprint.

We next studied whether compressing the time domain would bear additional benefits. In more detail, we rescaled all neuronal time constants in the network. For a scaling factor of 4 corresponding to $\tau_{\text{mem}} = 80$ ms and $\tau_{\text{syn}} = 40$ ms, the manipulation led to a marked reduction of overfitting that also resulted in a higher test accuracy of $(79.9 \pm 2.8)\%$ (Figure 8c).

As an alternative means to reduce overfitting, we sought to explore noise injection at the input layer. Specifically, we implemented event-based spike jitter across channels by adding a random number $\mathcal{N}(0, \sigma_u)$ to the unit index i of every input spike, which was then rounded to the nearest integer. We found that such input noise was effective in decreasing overfitting. For instance, a value $\sigma_u = 20$ led to an increased test accuracy of $(78.7 \pm 2.2)\%$ (Figure 8d).

When combined, the aforementioned strategies resulted in a further improved *best effort* test accuracy of $(83.2 \pm 1.3)\%$ on the SHD test set (Table 1). This is not only noticeably higher than the previous result of $(71.4 \pm 1.9)\%$ obtained by the RSNN, but also exceeds the effect of every contribution on its own.

Finally, to relate our LIF neurons to other work on RSNNs, we also evaluated the performance of the spiking neural units (SNUs) [Woźniak et al., 2020] on SHD. Although closely related to our LIF neuron model, SNUs feature delta synapses and rely on a different surrogate

Table 1: Performance comparison

	Architecture	SHD	SSC
SVM	Linear	56.0 \pm 0.4	21.6 \pm 0.0
	Poly-2	48.3 \pm 0.2	23.0 \pm 0.0
	Poly-3	46.7 \pm 0.5	23.9 \pm 0.0
	RBF	60.0 \pm 0.3	29.5 \pm 0.0
LSTM ¹		89.0 \pm 0.2	73.0 \pm 0.1
CNN		92.4 \pm 0.7	77.7 \pm 0.2
Spiking ¹	1-layer	48.1 \pm 1.6	32.5 \pm 0.5
	2-layer	48.6 \pm 0.9	38.5 \pm 0.6
	3-layer	47.5 \pm 2.3	41.0 \pm 0.5
	Recurrent	71.4 \pm 1.9	50.9 \pm 1.1
	Recurrent (best effort) ²	83.2 \pm 1.3	
	SNU ²	79.0 \pm 1.6	

¹ Trained with max-over-time loss

² 1024 neurons + data augmentation (optimized time constants and channel number combined with noise injection)

derivative. When trained under the same conditions as our *best effort* network, the SNU network reached a test accuracy of (79.0 \pm 1.6) % (Table 1) which is slightly lower than networks using our LIF neuron model.

4 Discussion

In this article, we introduced two new public domain spike-based classification datasets to facilitate the quantitative comparison of SNNs. Further, we provide a first set of baselines for future comparisons by training a range of spiking and non-spiking classifiers.

With these developments we address a lack of comprehensive benchmark datasets for SNNs. To advance the neuromorphic computing field, we need a set of benchmarks that pose real-world challenges to quantify gains and standardize evaluation across different platforms [Davies, 2019]. We view the datasets in this article as our contribution toward this goal. But, since it is difficult to foresee the pace of future developments, we acknowledge that the present datasets may not prove final. Thus, to facilitate their refinement, extension, and the creation of novel datasets, we released in addition to the spiking data, our conversion software³ and raw audio datasets², both under permissive public domain licenses.

Both spiking datasets are based on auditory classification tasks but were derived from data that was acquired in different recording settings. We chose audio data sets as the basis for our benchmarks because audio has a temporal dimension which makes it a natural choice for spike-based processing. However, in contrast to movie data, audio requires fewer input channels for a faithful representation, which renders the derived spiking datasets computationally more tractable.

We did not use one of the other existing audio datasets as a basis for the spiking version for different reasons. For instance, a large body of spoken digits is provided by the TIDIGITS dataset [Leonard and Doddington, 1991]. However, this dataset is only available under a commercial license and we were aiming for fully open datasets. In contrast, the Free Spoken Digit Dataset [Zohar et al., 2018] is available under Creative Commons BY 4.0 license. Since this dataset only contains 2k recordings with an overall lower recording and alignment quality, we deemed recording HD as a necessary contribution.

Other datasets, such as Mozilla’s Common Voice [Mozilla, 2019], LibriSpeech [Panayotov et al., 2015], and TED-LIUM [Rousseau et al., 2012] are also publicly available. However, these datasets pose more challenging speech detection problems since they are only aligned at the sentence level. Such more challenging tasks are left for future research on functional SNNs. The Spoken Wikipedia Corpora [Köhn et al., 2016], for instance, also provides alignment at the word level, but requires further preprocessing such as the dissection of audio files into separate words. Moreover, the pure size and imbalance in samples per class render the dataset more challenging. We therefore left its conversion for future work.

The only existing public domain dataset with word-level alignment, tractable size, and preprocessing requirements that we were aware of at the time of writing this manuscript was the SC dataset. This is the reason why we chose to base one spiking benchmark on SC while simultaneously providing the separate and the smaller HD dataset with higher recording quality and alignment precision. Finally, the high-fidelity recordings of the HD also make it suitable for quantitative evaluation of the impact of noise on network performance, because well-characterized levels of noise can be added.

The spike conversion step consists of a published physical inner-ear model [Sieroka et al., 2006] followed by an established hair-cell model [Meddis, 1988]. The processing chain is completed by a single layer of BCs to increase phase-locking and to decrease the overall number of spikes. This approach is similar to the publicly available DASDIGNET dataset [Anumula et al., 2018]. DASDIGNET is composed of recordings from the TIDIGIT dataset [Leonard and Doddington, 1991] which have been played to a dynamic audio sensor with 2×64 frequency selective channels. In contrast to SHD and SSC, the raw audio files of the TIDIGIT dataset are only available under a commercial license. Also, the frequency resolution, measured in frequency selective bands of the BM model, is about a factor of 10 lower. As the software used for processing SHD and SSC datasets is publicly available, it is straight forward to extend the present datasets. This step is more difficult for DASDIGNET, because it requires a dynamic audio sensor.

We standardize the conversion step from raw audio signals to spikes by generating spikes from the HD and the SC audio datasets. In doing so, we both improve the usability settings and reduce a common source of performance variability due to differences in the preprocessing pipelines of the end-user.

To establish the first set of baselines (Table 1), we trained a range of non-spiking and spiking classifiers on both the SHD as well as the SSC. In comparing the performance on the full datasets with performance obtained on reduced spike count datasets, we found that the temporal information available in the spike times can be leveraged for better classification by suitable classifiers. Moreover, architectures with explicit recurrence, like LSTMs and RSNNs, were the best performing models among all architectures we tested. Most likely, the reverberating activity through recurrent connections implements the required memory, thereby bridging the gap between neural time

constants and audio features. Therefore, the inclusion of additional state variables evolving on a slower time scale as in Bellec et al. [2018] will be an interesting extension to improve performance of SNNs.

In the present manuscript, we trained SNNs using surrogate gradients in combination with BPTT [Bellec et al., 2018; Shrestha and Orchard, 2018; Woźniak et al., 2020; Neftci et al., 2019; Bohte, 2011; Yin et al., 2020]. However, it is essential to realize that there exists a plethora of alternative gradient-based approaches based on network translation [Pfeiffer and Pfeil, 2018; Zambrano et al., 2017; Rückauer et al., 2019; Stöckl and Maass, 2020], single spike timing [Mostafa, 2018; Göltz et al., 2019], mean firing rate [Hunsberger and Eliasmith, 2015; Lee et al., 2019], and stochastic approximations [Gardner and Grüning, 2016; Bengio et al., 2013; Rezende and Gerstner, 2014; Jang et al., 2019]. Further, there are biologically inspired online approximations of surrogate gradients [Zenke and Ganguli, 2018; Kaiser et al., 2020; Bellec et al., 2020] and, finally, a body of work has used biologically motivated spike-timing dependent plasticity (STDP)-like learning rules [Kheradpisheh et al., 2018; Zhang et al., 2018] (see Tavanaei et al. [2018] for a comprehensive review). An in-depth comparison of this plethora of approaches was beyond the scope of this manuscript. However, the present datasets might prove useful in facilitating a more detailed comparison of the work mentioned above. As such, it is left as interesting future work to study how STDP interacts with the present datasets.

Our analysis of SHD and SSC using LSTMs and SNNs showed that the choice of loss functions can have a marked effect on classification performance. While LSTMs perform best with a last-time-step loss, in which only the last time step is used to calculate the cross entropy loss, SNNs achieved their highest accuracy for a max-over-time loss, in which the maximum membrane potential of each readout unit is considered. A detailed analysis of suitable cost functions for training SNNs is an interesting direction for future research.

In summary, we have introduced two versatile and open spiking datasets and conducted a first set of performance measurements using SNN classifiers. This constitutes an important step forward toward the more quantitative comparison of functional SNNs in-silico both on conventional computers and neuromorphic hardware.

A Inner ear model

Audio data were converted into spikes using a model of the inner ear and the ascending auditory pathway (cf. Figure 2) which combines a basilar membrane (BM) model with a population of hair cells (HCs) followed by a population of bushy cells (BCs) for spike generation. We now describe the model components individually.

A.1 Basilar membrane model

As a complete consideration of hydrodynamic BM models is beyond the scope of this manuscript, we closely follow the steps of Sieroka et al. [2006] and highlight the key steps

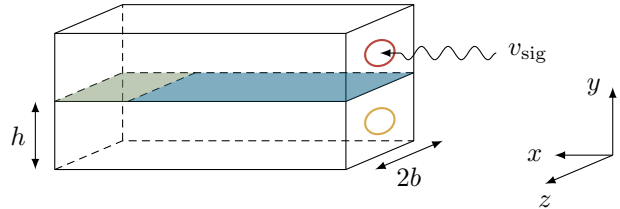


Figure 9: Schematic view of the basilar membrane model. The BM (blue) separates the *scala tympani* (lower chamber) from the *scala vestibuli* (upper chamber). At the *helicotrema* (green), the two scalae are connected. The *scala tympani* ends in the *round window* (yellow). A sound wave v_{sig} is penetrating the eardrum, applying pressure at the *oval window* (red) by moving the *ossicles*, leading to a compression and slower traveling wave. We have neglected the *scala media* [Sieroka et al., 2006] and consider a stretched form.

of their derivation. A fundamental aspect of a cochlea model is the interaction between a fluid and a membrane causing spatial frequency dispersion [Sieroka et al., 2006; de Boer, 1980, 1984]. Key mechanical features of the cochlea are covered by the simplified geometry of the BM in Figure 9. Here, we assumed the fluid to be inviscid and incompressible. Furthermore, we expect the oscillations to be small that the fluid can be described as linear. The BM was expressed in terms of its mechanical impedance $\xi(x, \omega)$ which depends on the position in the x -direction and the angular frequency $\omega = 2\pi\nu$:

$$\xi(x, \omega) = \frac{1}{i\omega} [S(x) - \omega^2 m + i\omega R(x)] , \quad (12)$$

with a transversal stiffness $S(x) = C_0 e^{-\alpha x} - a$, a resistance $R(x) = R_0 e^{-\alpha x/2}$ and an effective mass m [de Boer, 1980]. The damping of the BM was described by $\gamma = R_0 / \sqrt{C_0 m}$. Variations of the stiffness over several orders of magnitude allowed to encompass the entire range of audible frequencies.

Let $p(\mathbf{x}, \omega)$ be the difference between the pressure in the upper and lower chamber. The following expression fulfills the boundary conditions $v_y = 0$ for $y = h$, and $v_z = 0$ at $z = \pm b$ [de Boer, 1980]:

$$p(\mathbf{x}, \omega) = \sum_n \int_0^\infty \frac{dk}{2\pi} e^{-ikx} p_0(k) \left[\frac{\cosh(m_0(h-y))}{\cosh(m_0 h)} + \frac{m_0 \tanh(m_0 h) \cosh(m_1(h-y))}{m_1 \tanh(m_1 h) \cosh(m_1 h)} \cdot \cos\left(\frac{\pi z n}{b}\right) \right] . \quad (13)$$

The Laplace equation yields expressions for $m_0 = k$ and $m_1 = \sqrt{k^2 + \pi^2/b^2}$. Only the principal mode of excitation in the z -direction was considered by setting $n = 1$. With the assumptions made above, the Euler equation reads for the y -component of the velocity in the middle of the BM:

$$\partial_y p(x, \omega) = -i\omega \rho v_y(x, \omega) = \frac{2i\omega \rho}{\xi(x, \omega)} p(x, \omega) , \quad (14)$$

where we dropped the y and z argument for readability. In the following, we consider the limiting case of long waves

with $kh \ll 1$. By combining Equations (13) and (14), one gets:

$$\partial_x^2 p(x, \omega) = \frac{i\omega\rho}{h\xi(x, \omega)} p(x, \omega), \quad (15)$$

where the replacement $\hat{p}(k) \rightarrow p(x)$, $k \rightarrow i\partial_x$ and $k^2 \rightarrow \partial_x^2$ has been applied. Here, $\hat{p}(k)$ denotes the Fourier transform of $p(x, 0, 0)$. The solution of this equation was approximated by:

$$p(x, \omega) = \sqrt{\frac{G(x, \omega)}{g(x, \omega)}} H_0^{(2)}(G(x, \omega)), \quad (16)$$

where $H_0^{(2)}$ is the second Hankel function and $g(x, \omega)$ and $G(x, \omega)$ are given by:

$$g(x, \omega) = \omega \sqrt{\frac{\rho}{h\xi(x, \omega)}}, \quad (17)$$

$$G(x, \omega) = \int_0^x dx' g(x', \omega) + \frac{2}{\alpha} g(0, \omega). \quad (18)$$

An analytical expression for $G(x, \omega)$ can be found in Sieroka et al. [2006]. The model was applied to a given stimulus by:

$$v_y(x, t) = \int \frac{d\omega}{2\pi} i Z_{\text{in}} \frac{v_y(x, \omega)}{p(0, \omega)} e^{-i\omega t} v_{\text{sig}}(\omega), \quad (19)$$

where $v_{\text{sig}}(\omega)$ is the Fourier transformation of the stimulus. The input impedance of the cochlea was modeled by:

$$Z_{\text{in}}(\omega) = \frac{p(x=0)}{v_x(x=0)} \approx \sqrt{\frac{2C_0 i J_0(\zeta) + Y_0(\zeta)}{h J_1(\zeta) - i Y_1(\zeta)}}, \quad (20)$$

with the Bessel functions of first J_β and second Y_β kind of order β and $\zeta = 2\omega/\alpha\sqrt{2/(hC_0)}$.

To process the audio data, we evaluated $v_y(x, t)$ in the range $(0, 3.5 \text{ cm}]$ in N_{ch} steps of equal size. Specifically, we chose $N_{\text{ch}} = 700$ as a compromise between a faithful representation of the underlying audio signal and manageable computational cost when using the dataset. Before applying the BM model, each recording $v_{\text{sig}}(t)$ was normalized to a root mean square (RMS) value of 0.3 cm s^{-1} .

A.2 Hair cell model

The transformation of the movement of the BM to spikes was realized by the HC. The following description illustrates the key steps of Meddis [1986], to which we refer for further details.

In the HC model, one assumes that the cell contains a specific amount of free transmitter molecules $q(x, t)$ which could be released by use of a permeable membrane to the synaptic cleft (Figure 10). The permeability is a function of the velocity of the BM, $v_y(x, t)$:

$$k(x, t) = \begin{cases} \frac{g \cdot [c \cdot v_y(x, t) + A]}{c \cdot v_y(x, t) + A + B} & \text{for } v_y(x, t) + A > 0 \\ 0 & \text{else} \end{cases}. \quad (21)$$

The amount $c(x, t)$ of transmitter in the cleft is subject to chemical destruction or loss through diffusion $l \cdot c(x, t)$ as well as re-uptake into the cell $r \cdot c(x, t)$:

$$\frac{dc}{dt} = k(x, t)q(x, t) - l \cdot c(x, t) - r \cdot c(x, t). \quad (22)$$

Table 2: Model parameters

Parameter	Symbol	Value
Damping const.	γ	0.15 s^{-1}
Greenwoods const.	a	$35 \text{ kg s}^{-2} \text{ cm}^{-2}$
Stiffness const.	C_0	$10^9 \text{ g s}^{-2} \text{ cm}^{-2}$
Fluid density	ρ	1.0 g cm^{-3}
Attenuation factor	α	3.0 cm^{-1}
Height of scala	h	0.1 cm
Effective mass	m	0.05 g cm^{-2}
Number of channels	N_{ch}	700
Input scaling factor	c	1.0 s cm^{-1}
Permeability offset	A	5
Permeability rate	B	300
Maximum permeability	g	1000
Replenishing rate	y	11.11
Loss rate	l	1250
Reuptake rate	r	16 667
Reprocessing rate	n	250
Propability scaling	h	50 000
Number of HCs at same position	N_{HC}	40
Synaptic time const.	τ_{syn}	0.5 ms^1
Membrane time const.	τ_{mem}	1 ms^1
Refractory time const.	τ_{ref}	1 ms^1
Leak potential	u_{leak}	0
Reset potential	u_{reset}	0
Threshold potential	u_{thres}	1
Number of neurons per layer	N	128
Simulation step size	δt	0.5 ms
Simulation duration	T	1.0 s
Batch size	N_{batch}	256
Learning rate	η	0.001
Steepness of gradient	β	100
Regularization lower threshold	θ_l	0.01
Regularization lower strength	s_l	1.0
Regularization upper threshold	θ_u	100.0
Regularization upper strength	s_u	0.06
First moment estimates decay rate	β_1	0.9
Second moment estimates decay rate	β_2	0.999

¹ BC parameter

² SNN parameter

A fraction $n \cdot w(x, t)$ of the reuptaken transmitter $w(x, t)$ is continuously transferred to the free transmitter pool:

$$\frac{dw}{dt} = r \cdot c(x, t) - n \cdot w(x, t). \quad (23)$$

The transmitter originates in a manufacturing base that replenishes the free transmitter pool at a rate $y[1 - q(x, t)]$:

$$\frac{dq}{dt} = y[1 - q(x, t)] + n \cdot w(x, t) - k(x, t)q(x, t) \quad (24)$$

While in the cleft, transmitter quanta have a finite probability $\mathcal{P}_{\text{spike}} = h \cdot c(x, t) dt$ of influencing the post-synaptic excitatory potential. A refractory period was imposed by denying any event which occurs within 1 ms of a previous event. At each position x of the BM, we simulated $N_{\text{HC}} = 40$ independent HCs.

A.3 Bushy cell model

The phase-locking of HC outputs was increased by feeding their spike output to a population of N_{ch} BCs. In contrast to [Rothman et al., 1993], we implemented the BCs as standard LIF neurons. In more detail, we considered a single layer ($l = 1$) of BCs without recurrent connections ($V_{ij}^{(l)} = 0 \forall i, j$). The feed-forward weights were set to $W_{ij}^{(l)} = 0.54/N_{\text{HC}} \forall i, j$. A single BC was used to integrate the spiketrains of the $N_{\text{HC}} = 40$ HCs for each channel of the BM.

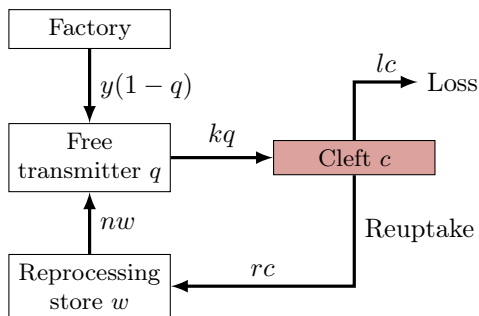


Figure 10: Schematic view of the transmitter flow within the hair cell (HC) model proposed. Figure adapted from Meddis [1986]. The model comprises four transmitter pools which allow to describe the transmitter concentration in the synaptic cleft.

B Non-spiking classifiers

For validation purposes, we applied three standard non-spiking methods for time-series classification to the datasets, namely SVMs, LSTMs, and CNNs. We give details on each of them in the following.

B.1 Support vector machines

We trained linear and non-linear SVMs using *scikit-learn* [Pedregosa et al., 2011]. Specifically, we trained SVMs with polynomial (up to third degree) and RBF kernels. The vectors in the input space were constructed such that for each sample a N_{ch} -dimensional vector \mathbf{x}_i is generated by counting the number of spikes emitted by each BC in each sample. Furthermore, features were standardized by removing the mean and scaling to the unit variance.

B.2 Long short term memories

We used LSTMs for validation purposes of the temporal data [Hochreiter and Schmidhuber, 1997]. The inputs to the LSTM consist of the N_{ch} spike trains emitted by the BCs, but binned in time bins of size 10 ms. We trained LSTM networks using *TensorFlow 1.14.0* with the *Keras 2.3.0* application programming interface (API) [Abadi et al., 2015; Chollet et al., 2015]. For all used layers, we stuck to the default parameters and initialization unless mentioned otherwise. Specifically, we considered a single LSTM layer with 128 cells with a dropout probability of 0.2 for the linear transformation of the input as well as for the linear transformation of the recurrent states. Last, a readout with softmax activation was applied. The model was trained with the Adamax optimizer [Kingma and Ba, 2014] and a categorical cross entropy loss defined on the activation of the last time step and the time step with maximal activation.

B.3 Convolutional neural networks

We applied CNNs to further test for separability of the datasets. To that end, the spike trains were not only

binned in time, but also in space. The temporal bin-width was set to 10 ms. Along the spatial dimension, the data was binned to result in 64 distinct input units. As for LSTMs, CNN networks were trained using *TensorFlow* with the *Keras* APIs with default parameters and initialization unless mentioned otherwise. First, a 2D convolution layer with 32 filters of size 11×11 and rectified linear unit (ReLU) activation function was applied. Next, the output was processed by 3 successive blocks, each composed of two 2D convolutional layers, each of them accompanied by batch normalization and ReLU activation. Both convolutional layers contain 32 filters of size 3×3 . We finalized the blocks by a 2D max-pooling layer with pool size 2×2 and a dropout layer with rate 0.2. The output of the last of the three blocks was processed by a dense layer with 128 nodes and ReLU activation function followed by a readout with softmax activation. The whole model is trained with the Adamax optimizer [Kingma and Ba, 2014] and a categorical cross entropy loss for optimization.

Acknowledgments

This work has received funding from the European Union Sixth Framework Programme ([FP6/2002-2006]) under grant agreement no 15879 (FACETS), the European Union Seventh Framework Programme ([FP7/2007-2013]) under grant agreement no 604102 (HBP), 269921 (Brain-ScaleS) and 243914 (Brain-i-Nets) and the Horizon 2020 Framework Programme ([H2020/2014-2020]) under grant agreement no 720270 and 785907 (HBP) as well as the Manfred Stärk Foundation. The authors acknowledge support by the state of Baden-Württemberg through bwHPC and the German Research Foundation (DFG) through grant no INST 39/963-1 FUGG (bwForCluster NEMO). This work was supported by the Novartis Research Foundation. Prof. Dr. Sebastian Hoth is acknowledged for enabling access to the sound-shielded room at the university hospital Heidelberg. Prof. Dr. Hans Günter Dosch is acknowledged for discussions and advice on auditory preprocessing. David Schumann is acknowledged for mastering the audio files of HD.

References

- Kwabena Boahen. A neuromorph’s prospectus. *Computing in Science Engineering*, 19(2):14–28, Mar 2017. doi: 10.1109/MCSE.2017.33.
- Friedemann Zenke and Surya Ganguli. SuperSpike: Supervised Learning in Multilayer Spiking Neural Networks. *Neural Computation*, 30(6):1514–1541, April 2018. ISSN 0899-7667. doi: 10.1162/neco_a_01086.
- Michael Pfeiffer and Thomas Pfeil. Deep Learning With Spiking Neurons: Opportunities and Challenges. *Front. Neurosci.*, 12, 2018. ISSN 1662-453X. doi: 10.3389/fnins.2018.00774.
- Amirhossein Tavanaei, Masoud Ghodrati, Saeed Reza Kheradpisheh, Timothée Masquelier, and Anthony

- Maida. Deep learning in spiking neural networks. *Neural Netw*, December 2018. ISSN 0893-6080. doi: 10.1016/j.neunet.2018.12.002.
- Guillaume Bellec, Darjan Salaj, Anand Subramoney, Robert Legenstein, and Wolfgang Maass. Long short-term memory and learning-to-learn in networks of spiking neurons. In *Advances in Neural Information Processing Systems*, pages 787–797, 2018.
- Sumit Bam Shrestha and Garrick Orchard. SLAYER: Spike Layer Error Reassignment in Time. In S. Bengio, H. Wallach, H. Larochelle, K. Grauman, N. Cesa-Bianchi, and R. Garnett, editors, *Advances in Neural Information Processing Systems 31*, pages 1419–1428. Curran Associates, Inc., 2018.
- Stanisław Woźniak, Angeliki Pantazi, Thomas Bohnstingl, and Evangelos Eleftheriou. Deep learning incorporating biologically inspired neural dynamics and in-memory computing. *Nature Machine Intelligence*, 2(6): 325–336, June 2020. ISSN 2522-5839. doi: 10.1038/s42256-020-0187-0. URL <https://www.nature.com/articles/s42256-020-0187-0>. Number: 6 Publisher: Nature Publishing Group.
- Emre O. Neftci, Hesham Mostafa, and Friedemann Zenke. Surrogate Gradient Learning in Spiking Neural Networks. *arXiv:1901.09948 [cs, q-bio]*, January 2019. arXiv: 1901.09948.
- J. Schemmel, D. Brüderle, A. Grübl, M. Hock, K. Meier, and S. Millner. A wafer-scale neuromorphic hardware system for large-scale neural modeling. *Proceedings of the 2010 IEEE International Symposium on Circuits and Systems (ISCAS'10)*, pages 1947–1950, 2010.
- Simon Friedmann, Johannes Schemmel, Andreas Grübl, Andreas Hartel, Matthias Hock, and Karlheinz Meier. Demonstrating hybrid learning in a flexible neuromorphic hardware system. *IEEE transactions on biomedical circuits and systems*, 11(1):128–142, 2016.
- S. B. Furber, D. R. Lester, L. A. Plana, J. D. Garside, E. Painkras, S. Temple, and A. D. Brown. Overview of the spinnaker system architecture. *IEEE Transactions on Computers*, 62(12):2454–2467, Dec 2013. ISSN 0018-9340. doi: 10.1109/TC.2012.142.
- M. Davies, N. Srinivasa, T. Lin, G. Chinya, Y. Cao, S. H. Choday, G. Dimou, P. Joshi, N. Imam, S. Jain, Y. Liao, C. Lin, A. Lines, R. Liu, D. Mathaikutty, S. McCoy, A. Paul, J. Tse, G. Venkataramanan, Y. Weng, A. Wild, Y. Yang, and H. Wang. Loihi: A neuromorphic manycore processor with on-chip learning. *IEEE Micro*, 38(1):82–99, January 2018. ISSN 0272-1732. doi: 10.1109/MM.2018.112130359.
- Saber Moradi, Ning Qiao, Fabio Stefanini, and Giacomo Indiveri. A scalable multicore architecture with heterogeneous memory structures for dynamic neuromorphic asynchronous processors (dynaps). *IEEE transactions on biomedical circuits and systems*, 12(1):106–122, 2018.
- Kaushik Roy, Akhilesh Jaiswal, and Priyadarshini Panda. Towards spike-based machine intelligence with neuromorphic computing. *Nature*, 575(7784):607–617, November 2019. ISSN 1476-4687. doi: 10.1038/s41586-019-1677-2. URL <https://www.nature.com/articles/s41586-019-1677-2>.
- Mike Davies. Benchmarks for progress in neuromorphic computing. *Nature Machine Intelligence*, 1(9):386–388, 2019.
- Yann LeCun, Léon Bottou, Yoshua Bengio, Patrick Haffner, et al. Gradient-based learning applied to document recognition. *Proceedings of the IEEE*, 86(11): 2278–2324, 1998.
- Joel Zylberberg, Jason Timothy Murphy, and Michael Robert DeWeese. A Sparse Coding Model with Synaptically Local Plasticity and Spiking Neurons Can Account for the Diverse Shapes of V1 Simple Cell Receptive Fields. *PLoS Comput Biol*, 7(10):e1002250, October 2011. doi: 10.1371/journal.pcbi.1002250.
- Emre O. Neftci, Charles Augustine, Somnath Paul, and Georgios Detorakis. Event-driven random back-propagation: Enabling neuromorphic deep learning machines. *Frontiers in Neuroscience*, 11: 324, 2017. doi: 10.3389/fnins.2017.00324. URL <https://www.frontiersin.org/article/10.3389/fnins.2017.00324>.
- Alex Krizhevsky, Geoffrey Hinton, et al. Learning multiple layers of features from tiny images. Technical report, Citeseer, 2009.
- Yuval Netzer, Tao Wang, Adam Coates, Alessandro Bissacco, Bo Wu, and Andrew Y. Ng. Reading Digits in Natural Images with Unsupervised Feature Learning. 2011. URL http://ufldl.stanford.edu/housenumbers/nips2011_housenumbers.pdf.
- Robert Gütig. To spike, or when to spike? *Current Opinion in Neurobiology*, 25:134–139, April 2014. ISSN 0959-4388. doi: 10.1016/j.conb.2014.01.004.
- Sander M Bohte, Joost N Kok, and Han La Poutre. Error-backpropagation in temporally encoded networks of spiking neurons. *Neurocomputing*, 48(1):17–37, 2002.
- H. Mostafa. Supervised Learning Based on Temporal Coding in Spiking Neural Networks. *IEEE Transactions on Neural Networks and Learning Systems*, PP(99):1–9, 2018. doi: 10.1109/TNNLS.2017.2726060.
- Iulia M. Comsa, Krzysztof Potempa, Luca Versari, Thomas Fischbacher, Andrea Gesmundo, and Jyrki Alakuijala. Temporal coding in spiking neural networks with alpha synaptic function. *arXiv:1907.13223 [cs, q-bio]*, July 2019.
- Raoul-Martin Memmesheimer, Ran Rubin, Bence P. Ölveczky, and Haim Sompolinsky. Learning Precisely Timed Spikes. *Neuron*, 82(4):925–938, May 2014. ISSN 0896-6273. doi: 10.1016/j.neuron.2014.03.026.

- Aditya Gilra and Wulfram Gerstner. Predicting non-linear dynamics by stable local learning in a recurrent spiking neural network. *eLife Sciences*, 6:e28295, November 2017. ISSN 2050-084X. doi: 10.7554/eLife.28295.
- Wilten Nicola and Claudia Clopath. Supervised learning in spiking neural networks with FORCE training. *Nature Communications*, 8(1):2208, December 2017. ISSN 2041-1723. doi: 10.1038/s41467-017-01827-3.
- Dominik Thalmeier, Marvin Uhlmann, Hilbert J. Kappen, and Raoul-Martin Memmesheimer. Learning Universal Computations with Spikes. *PLOS Comput Biol*, 12(6):e1004895, June 2016. ISSN 1553-7358. doi: 10.1371/journal.pcbi.1004895.
- Chris Eliasmith and Charles H. Anderson. *Neural Engineering: Computation, Representation, and Dynamics in Neurobiological Systems*. A Bradford Book, Cambridge, Mass., new ed edition edition, August 2004. ISBN 978-0-262-55060-4.
- Sophie Denève and Christian K. Machens. Efficient codes and balanced networks. *Nat Neurosci*, 19(3):375–382, March 2016. ISSN 1097-6256. doi: 10.1038/nn.4243.
- L. F. Abbott, Brian DePasquale, and Raoul-Martin Memmesheimer. Building functional networks of spiking model neurons. *Nature Neuroscience*, 19(3):350–355, March 2016. doi: 10.1038/nn.4241.
- Dongsung Huh and Terrence J Sejnowski. Gradient descent for spiking neural networks. In *Advances in Neural Information Processing Systems*, pages 1433–1443, 2018.
- Filip Ponulak and Andrzej Kasiński. Supervised Learning in Spiking Neural Networks with ReSuMe: Sequence Learning, Classification, and Spike Shifting. *Neural Computation*, 22(2):467–510, October 2009. ISSN 0899-7667. doi: 10.1162/neco.2009.11-08-901.
- Jean-Pascal Pfister, Taro Toyozumi, David Barber, and Wulfram Gerstner. Optimal Spike-Timing-Dependent Plasticity for Precise Action Potential Firing in Supervised Learning. *Neural Computation*, 18(6):1318–1348, April 2006. ISSN 0899-7667. doi: 10.1162/neco.2006.18.6.1318.
- Răzvan V. Florian. The Chronotron: A Neuron That Learns to Fire Temporally Precise Spike Patterns. *PLOS ONE*, 7(8):e40233, August 2012. ISSN 1932-6203. doi: 10.1371/journal.pone.0040233.
- Ammar Mohemmed, Stefan Schliebs, Satoshi Matsuda, and Nikola Kasabov. Span: spike pattern association neuron for learning spatio-temporal spike patterns. *Int. J. Neur. Syst.*, 22(04):1250012, June 2012. ISSN 0129-0657. doi: 10.1142/S0129065712500128.
- Brian Gardner and André Grüning. Supervised Learning in Spiking Neural Networks for Precise Temporal Encoding. *PLOS ONE*, 11(8):e0161335, August 2016. ISSN 1932-6203. doi: 10.1371/journal.pone.0161335.
- Robert Gütig and Haim Sompolinsky. The tempotron: a neuron that learns spike timing-based decisions. *Nat Neurosci*, 9(3):420–428, March 2006. ISSN 1097-6256. doi: 10.1038/nm1643.
- P. Lichtsteiner, C. Posch, and T. Delbruck. A 128x128 120 dB 15us Latency Asynchronous Temporal Contrast Vision Sensor. *IEEE Journal of Solid-State Circuits*, 43(2):566–576, February 2008. ISSN 0018-9200. doi: 10.1109/JSSC.2007.914337.
- Jithendar Anumula, Daniel Neil, Tobi Delbruck, and Shih-Chii Liu. Feature Representations for Neuromorphic Audio Spike Streams. *Frontiers in neuroscience*, 12:23, 2018. ISSN 1662-453X. doi: 10.3389/fnins.2018.00023.
- Garrick Orchard, Ajinkya Jayawant, Gregory K. Cohen, and Nitish Thakor. Converting Static Image Datasets to Spiking Neuromorphic Datasets Using Saccades. *Front. Neurosci.*, 9, 2015. ISSN 1662-453X. doi: 10.3389/fnins.2015.00437.
- Arnon Amir, Brian Taba, David Berg, Timothy Melano, Jeffrey McKinstry, Carmelo Di Nolfo, Tapan Nayak, Alexander Andreopoulos, Guillaume Garreau, Marcela Mendoza, and others. A Low Power, Fully Event-Based Gesture Recognition System. In *Proceedings of the IEEE Conference on Computer Vision and Pattern Recognition*, pages 7243–7252, 2017.
- Pete Warden. Speech commands: A dataset for limited-vocabulary speech recognition. *arXiv preprint arXiv:1804.03209*, 2018.
- David Schumann. dev-core. <https://dev-core.org/>. Accessed: 2019-08-23.
- Paul Knysh and Yannis Korkolis. Blackbox: A procedure for parallel optimization of expensive black-box functions. *arXiv preprint arXiv:1605.00998*, 2016.
- Xuedong Huang, Alex Acero, Hsiao-Wuen Hon, and Raj Reddy. *Spoken Language Processing: A Guide to Theory, Algorithm and System Development*. Prentice Hall, 2001. ISBN 978-0-13-022616-7.
- Benjamin Cramer, Yannik Stradmann, Johannes Schemmel, and Friedemann Zenke. Heidelberg spiking datasets, 2019. URL <http://dx.doi.org/10.21227/51gn-m114>.
- Wulfram Gerstner and Werner M Kistler. *Spiking neuron models: Single neurons, populations, plasticity*. Cambridge university press, 2002.
- Kaiming He, Xiangyu Zhang, Shaoqing Ren, and Jian Sun. Delving deep into rectifiers: Surpassing human-level performance on imagenet classification. In *Proceedings of the IEEE international conference on computer vision*, pages 1026–1034, 2015.
- Adam Paszke, Sam Gross, Soumith Chintala, Gregory Chanan, Edward Yang, Zachary DeVito, Zeming Lin, Alban Desmaison, Luca Antiga, and Adam Lerer. Automatic differentiation in PyTorch. In *NIPS Autodiff Workshop*, 2017.

- Friedemann Zenke and Tim P. Vogels. The remarkable robustness of surrogate gradient learning for instilling complex function in spiking neural networks. *bioRxiv*, page 2020.06.29.176925, June 2020. doi: 10.1101/2020.06.29.176925. URL <https://www.biorxiv.org/content/10.1101/2020.06.29.176925v1>. Publisher: Cold Spring Harbor Laboratory Section: New Results.
- Diederik P Kingma and Jimmy Ba. Adam: A method for stochastic optimization. *arXiv preprint arXiv:1412.6980*, 2014.
- Yinghao Li, Robert Kim, and Terrence J. Sejnowski. Learning the synaptic and intrinsic membrane dynamics underlying working memory in spiking neural network models. *bioRxiv*, page 2020.06.11.147405, June 2020. doi: 10.1101/2020.06.11.147405. URL <https://www.biorxiv.org/content/10.1101/2020.06.11.147405v1>. Publisher: Cold Spring Harbor Laboratory Section: New Results.
- R Gary Leonard and George R Doddington. A speaker-independent connected-digit database. *Instruments Incorporated, Central Research Laboratories, Dallas, TX*, 75266, 1991.
- Jackson Zohar, Souza César, Flaks Jason, Pan Yuxin, Nicolas Hereman, and Thite Adhish. Jakobovski/free-spoken-digit-dataset: v1.0.8, August 2018. URL <https://doi.org/10.5281/zenodo.1342401>.
- Mozilla. Mozilla common voice, August 2019. URL <https://voice.mozilla.org/en>.
- Vassil Panayotov, Guoguo Chen, Daniel Povey, and Sanjeev Khudanpur. Librispeech: an asr corpus based on public domain audio books. In *2015 IEEE International Conference on Acoustics, Speech and Signal Processing (ICASSP)*, pages 5206–5210. IEEE, 2015.
- Anthony Rousseau, Paul Deléglise, and Yannick Esteve. Ted-lium: an automatic speech recognition dedicated corpus. In *LREC*, pages 125–129, 2012.
- Arne Köhn, Florian Stegen, and Timo Baumann. Mining the spoken wikipedia for speech data and beyond. In Nicoletta Calzolari (Conference Chair), Khalid Choukri, Thierry Declerck, Marko Grobelnik, Bente Maegaard, Joseph Mariani, Asuncion Moreno, Jan Odijk, and Stelios Piperidis, editors, *Proceedings of the Tenth International Conference on Language Resources and Evaluation (LREC 2016)*, Paris, France, may 2016. European Language Resources Association (ELRA). ISBN 978-2-9517408-9-1.
- N Sieroka, H G Dosch, and A Rupp. Semirealistic models of the cochlea. *The Journal of the Acoustical Society of America*, 120(1):297–304, 2006. ISSN 0001-4966. doi: 10.1121/1.2204438.
- R Meddis. Simulation of auditory–neural transduction: Further studies. *The Journal of the Acoustical Society of America*, 83(3):1056–1063, 1988.
- Sander M. Bohte. Error-Backpropagation in Networks of Fractionally Predictive Spiking Neurons. In *Artificial Neural Networks and Machine Learning – ICANN 2011*, Lecture Notes in Computer Science, pages 60–68. Springer, Berlin, Heidelberg, June 2011. ISBN 978-3-642-21734-0 978-3-642-21735-7. doi: 10.1007/978-3-642-21735-7_8. URL https://link.springer.com/chapter/10.1007/978-3-642-21735-7_8.
- Bojian Yin, Federico Corradi, and Sander M. Bohté. Effective and Efficient Computation with Multiple-timescale Spiking Recurrent Neural Networks. *arXiv:2005.11633 [cs]*, June 2020. URL <http://arxiv.org/abs/2005.11633>. arXiv: 2005.11633.
- Davide Zambrano, Roeland Nusselder, H. Steven Scholte, and Sander Bohte. Efficient Computation in Adaptive Artificial Spiking Neural Networks. *arXiv:1710.04838 [cs]*, October 2017. URL <http://arxiv.org/abs/1710.04838>. arXiv: 1710.04838.
- Bodo Rückauer, Nicolas Känzig, Shih-Chii Liu, Tobi Delbruck, and Yulia Sandamirskaya. Closing the Accuracy Gap in an Event-Based Visual Recognition Task. *arXiv:1906.08859 [cs]*, May 2019. URL <http://arxiv.org/abs/1906.08859>. arXiv: 1906.08859.
- Christoph Stöckl and Wolfgang Maass. Classifying Images with Few Spikes per Neuron. *arXiv:2002.00860 [cs]*, January 2020. URL <http://arxiv.org/abs/2002.00860>. arXiv: 2002.00860.
- Julian Göltz, Andreas Baumbach, Sebastian Billaudelle, Oliver Breitwieser, Dominik Dold, Laura Kriener, Akos Ferenc Kungl, Walter Senn, Johannes Schemmel, Karlheinz Meier, and Mihai Alexandru Petrovici. Fast and deep neuromorphic learning with time-to-first-spike coding. *arXiv:1912.11443 [cs, q-bio, stat]*, December 2019. URL <http://arxiv.org/abs/1912.11443>. arXiv: 1912.11443.
- Eric Hunsberger and Chris Eliasmith. Spiking Deep Networks with LIF Neurons. *arXiv:1510.08829 [cs]*, October 2015. URL <http://arxiv.org/abs/1510.08829>. arXiv: 1510.08829.
- Chankyu Lee, Syed Shakib Sarwar, and Kaushik Roy. Enabling Spike-based Backpropagation in State-of-the-art Deep Neural Network Architectures. *arXiv:1903.06379 [cs]*, August 2019. URL <http://arxiv.org/abs/1903.06379>. arXiv: 1903.06379.
- Yoshua Bengio, Nicholas Léonard, and Aaron Courville. Estimating or Propagating Gradients Through Stochastic Neurons for Conditional Computation. *arXiv:1308.3432 [cs]*, August 2013. URL <http://arxiv.org/abs/1308.3432>. arXiv: 1308.3432.
- Danilo Jimenez Rezende and Wulfram Gerstner. Stochastic variational learning in recurrent spiking networks. *Front. Comput. Neurosci.*, 8:38, 2014. doi: 10.3389/fncom.2014.00038. URL http://journal.frontiersin.org/Journal/10.3389/fncom.2014.00038/full?utm_source=newsletter&utm_medium=web&utm_campaign=Neuroscience-w18-2014.

- Hyeryung Jang, Osvaldo Simeone, Brian Gardner, and Andre Gruning. An Introduction to Probabilistic Spiking Neural Networks: Probabilistic Models, Learning Rules, and Applications. *IEEE Signal Processing Magazine*, 36(6):64–77, November 2019. ISSN 1558-0792. doi: 10.1109/MSP.2019.2935234. Conference Name: IEEE Signal Processing Magazine.
- Jacques Kaiser, Hesham Mostafa, and Emre Neftci. Synaptic Plasticity Dynamics for Deep Continuous Local Learning (DECOLLE). *Front. Neurosci.*, 14:424, May 2020. ISSN 1662-453X. doi: 10.3389/fnins.2020.00424. URL <http://arxiv.org/abs/1811.10766>. arXiv: 1811.10766 version: 4.
- Guillaume Bellec, Franz Scherr, Anand Subramoney, Elias Hajek, Darjan Salaj, Robert Legenstein, and Wolfgang Maass. A solution to the learning dilemma for recurrent networks of spiking neurons. *Nature Communications*, 11(1):3625, July 2020. ISSN 2041-1723. doi: 10.1038/s41467-020-17236-y. URL <https://www.nature.com/articles/s41467-020-17236-y>. Number: 1 Publisher: Nature Publishing Group.
- Saeed Reza Kheradpisheh, Mohammad Ganjtabesh, Simon J. Thorpe, and Timothée Masquelier. STDP-based spiking deep convolutional neural networks for object recognition. *Neural Networks*, 99:56–67, March 2018. ISSN 0893-6080. doi: 10.1016/j.neunet.2017.12.005. URL <http://www.sciencedirect.com/science/article/pii/S0893608017302903>.
- Tielin Zhang, Yi Zeng, Dongcheng Zhao, and Mengting Shi. A plasticity-centric approach to train the non-differential spiking neural networks. In *Thirty-Second AAAI Conference on Artificial Intelligence*, 2018.
- E de Boer. Auditory physics. Physical principles in hearing theory. I. *Physics reports*, 62(2):87–174, 1980.
- E de Boer. Auditory physics. Physical principles in hearing theory. II. *Physics Reports*, 105(3):141–226, 1984.
- R. Meddis. Simulation of mechanical to neural transduction in the auditory receptor. *The Journal of the Acoustical Society of America*, 79(3):702–711, 1986.
- Jason S Rothman, Eric D Young, and Paul B Manis. Convergence of auditory nerve fibers onto bushy cells in the ventral cochlear nucleus: implications of a computational model. *Journal of Neurophysiology*, 70(6): 2562–2583, 1993.
- F. Pedregosa, G. Varoquaux, A. Gramfort, V. Michel, B. Thirion, O. Grisel, M. Blondel, P. Prettenhofer, R. Weiss, V. Dubourg, J. Vanderplas, A. Passos, D. Cournapeau, M. Brucher, M. Perrot, and E. Duchesnay. Scikit-learn: Machine learning in Python. *Journal of Machine Learning Research*, 12:2825–2830, 2011.
- Sepp Hochreiter and Jürgen Schmidhuber. Long short-term memory. *Neural computation*, 9(8):1735–1780, 1997.
- Martín Abadi, Ashish Agarwal, Paul Barham, Eugene Brevdo, Zhifeng Chen, Craig Citro, Greg S. Corrado, Andy Davis, Jeffrey Dean, Matthieu Devin, Sanjay Ghemawat, Ian Goodfellow, Andrew Harp, Geoffrey Irving, Michael Isard, Yangqing Jia, Rafal Jozefowicz, Lukasz Kaiser, Manjunath Kudlur, Josh Levenberg, Dandelion Mané, Rajat Monga, Sherry Moore, Derek Murray, Chris Olah, Mike Schuster, Jonathon Shlens, Benoit Steiner, Ilya Sutskever, Kunal Talwar, Paul Tucker, Vincent Vanhoucke, Vijay Vasudevan, Fernanda Viégas, Oriol Vinyals, Pete Warden, Martin Wattenberg, Martin Wicke, Yuan Yu, and Xiaoqiang Zheng. TensorFlow: Large-scale machine learning on heterogeneous systems, 2015. URL <https://www.tensorflow.org/>. Software available from tensorflow.org.
- François Chollet et al. Keras. <https://keras.io>, 2015.